In-situ compression with acoustic emission detection of high pressure torsion deformed $Cu_{38}Zr_{54}Al_8$ metallic glass micropillars

Talaye Arjmandabasi [a], Dávid Ugi [a], Ádám Révész [a], Erhard Schafler [b], David J. Browne [c], Zsolt Kovács [a],*

[a] Department of Materials Physics, Eötvös Loránd University, Pázmány Péter st. 1/a, Budapest, Hungary
[b] Physics of Nanostructured Materials, Faculty of Physics, University of Vienna, A-1090 Vienna, Austria
[c] School of Mechanical and Materials Engineering, University College Dublin, Belfield Dublin 4, Ireland

ARTICLE INFO

ABSTRACT

In-situ compression of $Cu_{38}Zr_{54}Al_8$ metallic glass micropillars in a scanning electron microscope was performed together with continuous acoustic emission recording on samples in the as-cast state and after pre-deformation by high pressure torsion. A size effect was detected in both shear band operation and acoustic emission signal, irrespective of the preliminary deformation. This phenomenon was explained by the size dependent compliance of the pillar/indenter system. Differences between acoustic emission signals from the as-cast and pre-deformed states indicated changes in the shear band formation mechanism due to high pressure torsion. These differences were clear in the elastic regime of the in-situ compression and supported the role of rejuvenation in stabilization of unstable shear bands.

1. Introduction

Metallic glasses (MGs) are a special class of material, which lack long range order but have metallic characteristics with the ability to re-arrange their local atomic environments (via so-called shear transformation zones) under stress [1,2]. Metallic glasses have attracted considerable interest due to their disordered amorphous structure and distinctive mechanical properties, like high strength and superior elastic properties, good wear and corrosion resistance [3,4]. These special characteristics of MGs are basically related to the absence of defects and other structural features above the atomic scale. Intrinsic structure, which is free from the limitations of defects, makes MGs promising structural materials in applications having feature size as small as about ten nanometers [5].

Metallic glasses can be formed by rapid quenching from their liquid state, provided the cooling rate reaches a critical value at which the disordered liquid state solidifies without crystallization [6]. In recent decades, special alloys with low critical cooling rate were developed to form bulk metallic glasses (BMGs) having all dimensions larger than a millimeter [3]. Metallic glasses exhibit very different mechanical behavior in bulk state than in small size. Macroscopic MG samples mostly show instant fracture along a shear band (SB) in uniaxial

deformation tests [7]. Such a SB is a few nanometer (~10 nm) thick plane along which plastic deformation localizes [8]. This strain localization leads to poor macroscopic plasticity, i.e. to a brittle like behavior, with no ductility in conventional unconstrained deformation modes [9, 10]. However, MGs can also exhibit inherent plasticity, which can be revealed by inhomogeneous stresses and mechanical constraints. Notable plastic deformation can be reached in e.g., bending [11], torsion [12], by inducing a large number of SBs and dispersing the plastic strain. With increasing plastic deformation, plasticity first appears as serrations, later these serrations become less intense and finally they practically disappear as SB density increases continuously [12]. Accordingly, deformation methods producing high SB density can reveal plasticity in MGs. Shot peening and high-pressure torsion (HPT) are examples of such pre-deformation treatments, that have proved to produce plasticity [13, 14]. Among similar methods, HPT is routinely used to produce severe plastic deformation in various bulk crystalline samples [15,16] and also in several MG [17–20] and BMG samples [21–23]. In MG samples, stress inhomogeneities down to micrometer scale [24] and beyond [23] are produced by the high shear band density formed in HPT deformed BMG disks.

Deformation in small samples shows the same transition from brittle behavior to full plastic deformability (even in uniaxial tests) solely by

decreasing the sample size. Micropillars produced by focused ion beam (FIB) milling often exhibit serrations and gradual fracture along several SBs [25–28] Shear localization in such SBs is strongly influenced by decreasing the sample size, leading to the dramatically increased plasticity or even homogeneous flow in the submicrometer regime [26–28]. In details, three different size regimes (d) have been observed in MGs during deformation [29]. I) A macroscopic regime ($d > \sim10$ μm), in which a single SB appears and slips through the entire sample. II) A micron-sized regime (0.1 μm $< d < 10$ μm), in which transition occurs from single SB mode to multiple SB mode involving partial slips along SBs [26]. III) A nano regime ($d < \sim100$ nm), in which homogeneous plastic deformation can be observed [27]. Beside sample size, elastic modulus, temperature and other parameters also have effects on the serrations [30,31]. These effects can be well characterized by the stress drop amplitude and the strain burst speeds, due to the instability of plastic deformation in the propagating shear band [30].

As the size effect in MG materials usually shows itself in terms of shear banding, an explanation for size dependent deformation behavior was suggested via planar defect formation based on the Griffith theory by Volkert et al. [26]. In this theory, a high energy surface extends at the expense of available elastic energy of the system. Beyond a critical point, surface formation can accelerate and lead to sudden formation of a high energy defect plane, i.e. to the appearance of a SB. This modified Griffith theory predicts a critical sample size, based on the excess surface energy of a shear band. For various MGs, this critical size (cca 100 nm) is in agreement with the transition from homogeneous plastic deformation to localized shear banding between regimes II and III [25,26,32,33]. For larger samples, dynamics of the shear band propagation, casting defects and the interplay with elastic environment can explain the transition between regime I and II [33,34]. In situ information on the transition, other than the measured stress signal and surface imaging, is practically absent in the literature for micro deformation tests; therefore, the alternative information source of acoustic emission signal, which was successfully used for macroscopic deformation tests in BMG samples [35] and recently for micro-scale structures [36,37], is employed in the deformation tests on MG micro-pillars in the present work.

Acoustic emission (AE) signal measurement is a unique indirect experimental technique that provides real-time dynamic information on abrupt structural changes in materials. These structural changes emit elastic waves by the rapid energy release from mostly localized sources [38,39]. Since elastic waves can also be produced by the collective activation of plastic events, AE can give an insight into SB nucleation and propagation in MGs [35,40,41]. Strong AE events are mostly in exact correlation with the formation of large SBs in deforming BMGs as reported by Dalla Torre et al. [41]. Therefore, AE events precede stress drops and account for the structural rearrangements and localization of shear transformation zones during SB formation.

In this study, we present micro-compression tests with in-situ scanning electron microscope imaging on micropillars made of as-cast and pre-deformed Cu-Zr-Al metallic glasses. We investigate the effect of pillar size, and pre-deformation generated by HPTPZH by following distortions of micropillar shape and recording acoustic emission signal simultaneously.

2. Experimental methods

2.1. Sample preparation

Bulk metallic glass cylinder with $Cu_{38}Zr_{54}Al_8$ nominal composition and radius R= 3 mm was cast by suction casting into a Cu-mold in an arc furnace from liquid state under protective argon atmosphere [42,43]. Sample disks were prepared from the as-cast cylinder with a thickness of appr. 1 mm. A series of these disks were subjected to severe plastic deformation by HPT for various numbers of whole turns with an angular velocity of $\omega = 0.2\cdot2\pi$ rad/min under an applied pressure of 8 GPa at room temperature [44]. The HPT procedure was performed in

constrained mode using tools with cavities in both anvils [45]. In the present paper, we used a HPT disk with 5 whole turns and a reference as-cast BMG disk for in-situ local mechanical characterization. An optical micrograph taken on the surface of the HPT-disk is presented in Fig. 1. As one can see, there is some outflow of the material at the perimeter due to the reduction of the average sample thickness from 1.15 mm to 0.93 mm and adaption of sample to the anvil shape during compression and subsequent torsion in the constrained geometry. In order to monitor a possible slippage between the stainless steel anvils of the HPT apparatus and the BMG disk, a radial marker line has been drawn on the surface of the disk. The continuous marker line observed after the HPT-process confirms the lack of any significant slippage.

2.2. Micropillar preparation

Micropillars were prepared in both the as-cast and HPT deformed samples for the local mechanical tests in a FEI Quanta 3D dual beam scanning electron microscope (SEM). For both specimens, the pillar fabrication has been performed at approximately r~0.5 R from the torsion axis. To fabricate the pillars, the disks were cut and the cut surface of the disks were manually polished to 50 nm (Al_2O_3 polishing powder size) in order to have a clean and smooth surface for the milling. The samples were washed in acetone in an ultrasonic bath to get rid of contamination. Then micropillars were fabricated on the polished surface by Ga ion milling using FIB inside the SEM under vacuum. The milling process was carried out on each sample providing various sizes (a=4, 8, 12 μm) of square shaped pillars with proportional height (L) to have an aspect ratio of approximately L/a= 3. At first a thin hard layer of Pt cap was deposited to minimize the Ga ion contamination during milling and then the pillars were fabricated by FIB milling with gradually decreasing ion current. For imaging the sample preparation process and the subsequent in-situ compression test, secondary electron images were captured in the same SEM. Images of the early stage of fabrication and a completed pillar are shown in Fig. 2a and b, respectively.

2.3. Deformation tests and acoustic emission measurement

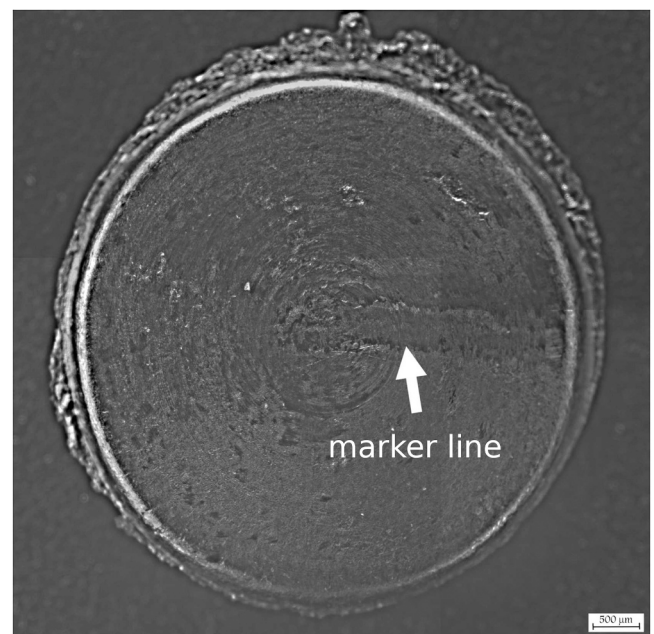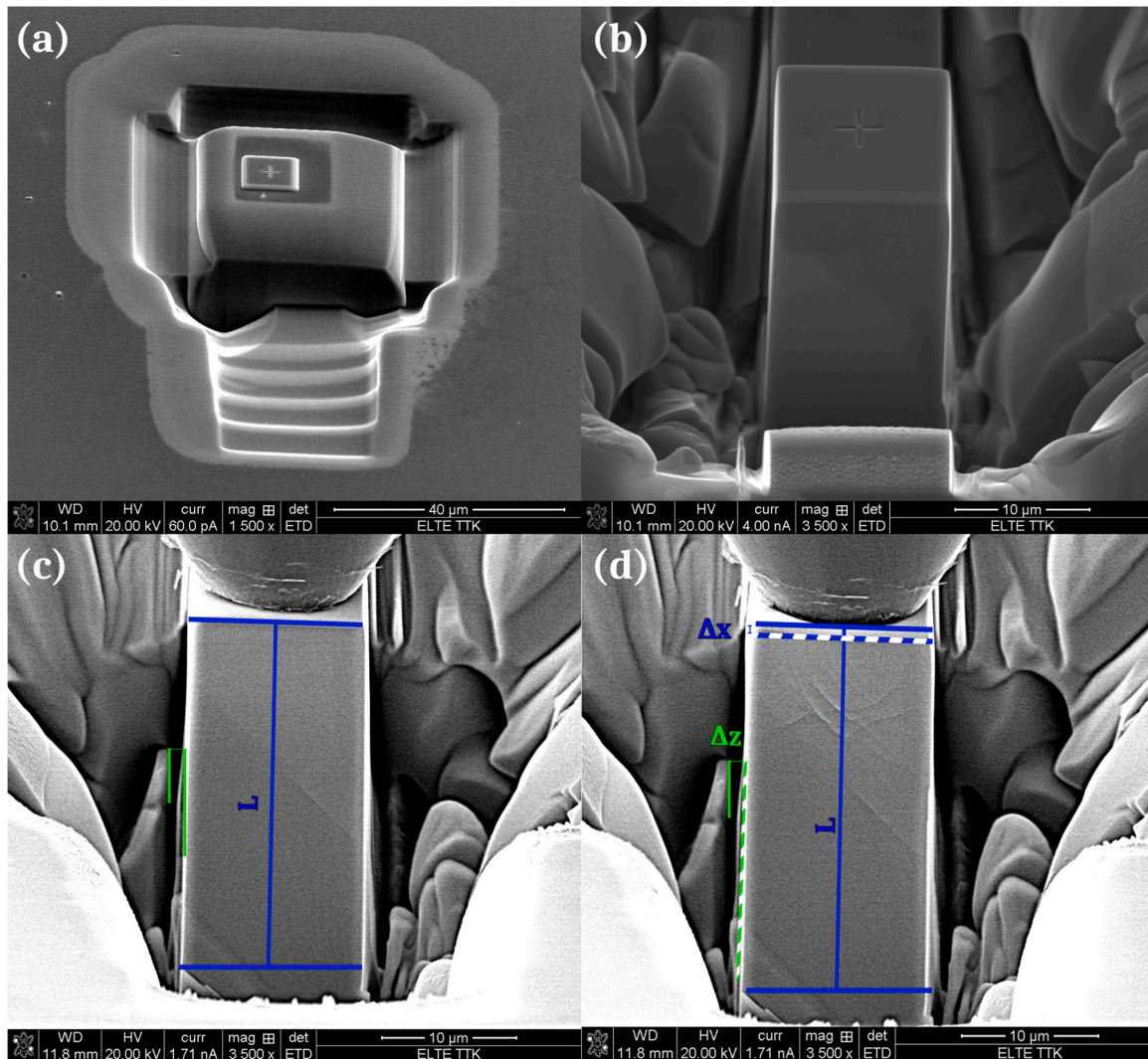In-situ micro compression tests were carried out in the same FEI

Fig. 1. Optical micrograph taken on the surface of the $Cu_{38}Zr_{54}Al_8$ BMG disk after HPT. Radial marker line has been drawn on the surface of the disk before the HPT process is also indicated.

Fig. 2. SEM images of different steps of the micropillar preparation and in-situ compression tests. (a) Early stage of the milling process. (b) Finished micropillar. (c) Initial and (d) a deformed state of the 12 μm micropillar in as-cast BMG during in-situ compression test. Evaluation lines for Δx in axis length change (blue) and Δz off axis misalignments (green) are indicated.

Quanta 3D SEM with an on-site built nanoindenter device and with continuous AE detection [37]. During micro compression tests, the platen velocity of the indenter was set proportionally (20, 40 and 60 nm/s) to the size of the micropillars (for samples a=4, 8, 12 μm, respectively) in order to get a constant nominal strain rate for all the measurements. Micropillars were compressed with a doped flat head diamond indenter, which was attached to the platen of the in-situ indenter by a soft elastic spring. Indenter displacement was determined from the platen position and from the elastic length change of the spring. In each micro compression test, indenter movement was reversed in few seconds after plastic strain of about ~0.1 was reached.

SEM images were captured continuously (with about 1–3 frame/s, 1024 ×943 resolution) during each compression test and these images were graphically evaluated to obtain an alternative "optical" deformation of the micropillars. As marked in Fig. 2c and d, evaluation lines for optical deformation readings are shown in selected SEM images. As an example, at one stage of the compression, the distance between the blue dashed and solid lines shows the in axis length change (Δx) of a compressed pillar. Off axis motion (Δz) of the pillars were also evaluated by measuring inclination which was indicated by the green markers in Fig. 2c and d. These parameters allowed to determine the $\varepsilon_{in}(t)= \Delta x/L$ in-axis and $\gamma(t)= \Delta z/L$ off-axis strains as a function of time. Additionally, the initial $\gamma(t = 0)$ pillar misalignment and γ_{taper} pillar taper (see

Table 1
Characteristic parameters of the pillars. Initial misalignment angle ($\gamma(t = 0)$), average taper (γ_{taper}), yeld stress (σ_{yield}) and compression modulus obtained from indenter displacement (E_{exp}).

Sample	γ (t = 0) (deg)	γ_{taper} (deg)	σ_{yield} (GPa)	E_{exp} (GPa)
as-cast 4 μm	1.3	0.0	2.32	50.9
as-cast 8 μm	0.9	0.1	1.83	33.2
as-cast12 μm	0.8	0.2	1.80	32.5
HPT 4 μm	3.2	0.8	2.55	16.9
HPT 8 μm	3.0	0.5	2.03	22.5
HPT 12 μm	3.3	0.8	2.22	27.6

Table 1) were determined with higher accuracy from the slopes of the visible edges of the pillars.

Acoustic signals were detected during the compression tests by a piezoelectric transducer which was attached to the back side of the samples. The nanoindenter device was equipped with a Physical Acoustics Corporation (PAC) WSα wide-band (100–1000 kHz) AE sensor, which showed a superior combination of frequency and sensitivity characteristics. Data acquisition and processing were performed by the computer controlled Vallen AMSY-6 system. AE events were identified in the continuous AE signal by a threshold value of 11 μV in all

cases.

3. Results

Uniaxial micro pillar compression tests were conducted at room temperature to investigate the size and pre-deformation dependence of mechanical properties in $Cu_{38}Zr_{54}Al_8$ BMG. Fig. 3, shows the compressed pillars in the as-cast (a-c) and the HPT deformed (d-f) states for various pillar sizes. As can be seen in the figures, shear band formation and slip planes are visible in all compression tests irrespective of the sample size and preliminary deformation. On the other hand, a clear indication on size effect can be observed for both the as-cast and HPT samples (Fig. 3). For 4 μm size pillars, deformation was stopped and reversed successfully before serious distortion of the original pillar geometry, while apparent changes in the pillar shape can be observed for 8 μm size pillars and sample pillar fracture occurred along one major shear band in both 12 μm size pillars. This indicates that the larger the pillar, the stronger the effect of a major shear band during the deformation process.

A stress-strain curve was plotted for each micro compression test in Fig. 4. As can be seen, all the deformation curves exhibit a general elastic–plastic behavior, but the smallest (4 μm size) pillars also poses several stress drops (serrations) of low amplitude. For the 12 μm size pillars, the amplitude of the stress drops becomes comparable to the yield strength and practically one serration dominates the plastic regime. This behavior is also an indication of the size effect, since the size of the pillar has a profound effect on the number of serrations. Such a strong and nearly instantaneous stress decay along one serration and in the same time the appearance of a single major shear band in Fig. 3c and f for 12 μm size pillars suggest generally that each serration along the stress-strain curve is caused by the formation of a single shear band.

Interestingly, the deformation characteristics are reproduced also for the HPT deformed samples irrespective of the sample dimensions (c.f.

Fig. 4a to b). However, the compression curves of the HPT pre-deformed samples show a specific feature which is absent for pillars prepared in the as-cast BMG. While deformation curves of the pillars in the as-cast state begin with an ordinary linear-elastic regime, the same part of the compression curves for HPT samples starts with a gradual increase in the slope (see the inset of Fig. 4b). Appearance of such a gradual slope change in compression tests is typical for sample/cross-head misalignment in macroscopic tests. In present tests, it can also have a similar explanation, however the different sample misalignment for HPT and as-cast pillars have a clear structural origin. All the pillars made of the as-cast sample have smaller distortions (even the 4 μm size pillars), at the same time visible misalignment and larger sample edge tapers were formed in the pillars made of the HPT samples (Table 1). This indicates that internal stresses were mainly relaxed at the length scale of pillars during the casting process, but subsequent HPT deformation induced strong and inhomogeneous stress field into the HPT sample.

During the micro-pillar compression tests, AE events were detected simultaneously. Correlation between the serrations and the AE signal can be observed for both the as-cast and the HPT samples as shown in Fig. 5. Specifically, the major AE events of the 4 μm pillars are mostly in coincidence with the load drops of the deformation curve as shown in Fig. 6, but no correlation was observed between the sizes of the serrations and the amplitudes of the corresponding AE signal Videos of the corresponding in-situ SEM compression tests for the as-cast (Video S1) and HPT (Video S2) samples are uploaded as supplementary material. Regarding the size of the micropillars, a gradual change in the AE signal is also visible in the elastic (microplastic) regime. Namely, in the as-cast sample, large AE events with $0.04\ mV < A_{AE} < 0.10\ mV$ amplitudes are visible before the yield point in the 12 μm pillar, while considerable smaller ($A_{AE} < 0.05\ mV$) events can be observed for the 8 μm pillar and practically no AE events emerge from the background noise for the smallest 4 μm pillar. The pillars in the HPT sample produce significantly less and smaller AE events in the elastic region without this size
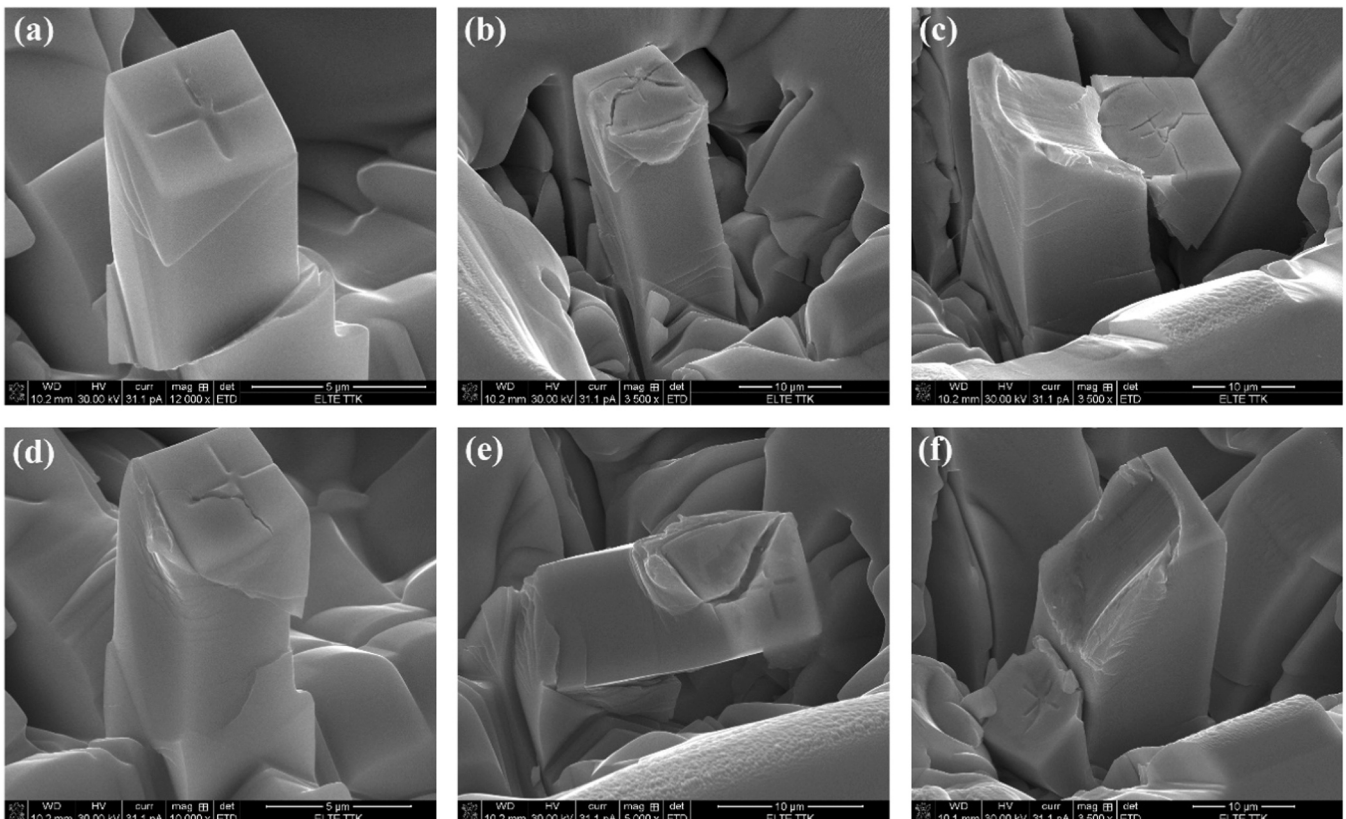

Fig. 3. SEM images of compressed as-cast 4–12 μm (a-c) and HPT deformed 4–12 μm (d-f) micropillars after unloading, respectively.
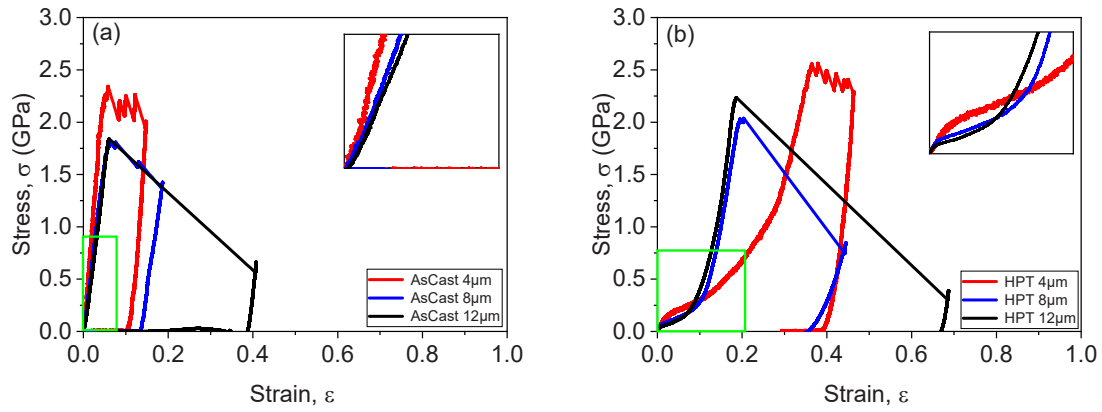
Fig. 4. Stress-strain curves of micro pillar compression for (a) as-cast and (b) HPT pre-deformed samples for various pillar sizes. Initial part of the stress-strain curves is magnified in the inset.
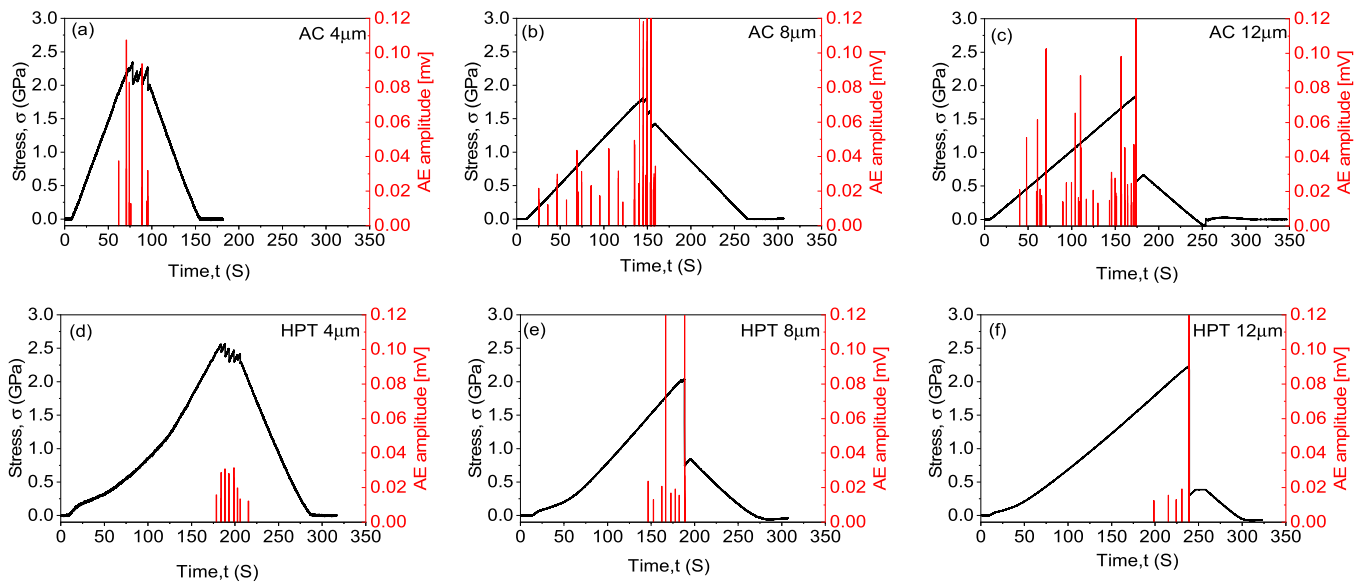

Fig. 5. Correlation between serrations of the deformation curve (black) and the amplitudes of the acoustic emission events (red) in micropillar compression tests for 4,8 and 12 μm pillars in as-cast (a-c) and HPT deformed samples (d-f), respectively.

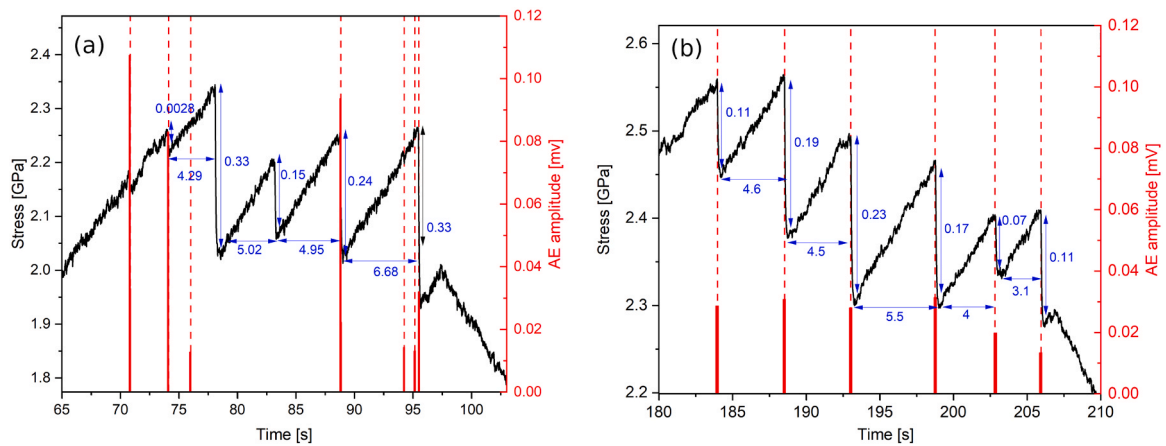

Fig. 6. Plastic regimes of the compression tests (black line) for the 4 μm size (a) as-cast and (b) HPT pre-deformed pillars. Timing and amplitudes of the AE events are indicated by dashed and solid vertical red lines, respectively.

dependent trend.

Supplementary material related to this article can be found online at doi:10.1016/j.jallcom.2023.171295.

Supplementary material related to this article can be found online at doi:10.1016/j.jallcom.2023.171295.

4. Discussion

4.1. Compression modulus and micropillar misalignment

By analyzing the deformation curves of the micropillar compression tests, the maximum stress (σ_{yield}) and elastic modulus (E_{exp}) of each sample were determined. In correlation with the change of deformation mode from single slip to multiple slip, the maximum stress of the 4 μm pillars is significantly higher than that of the larger pillars (Table 1). This is in qualitative agreement with a general strain gradient theory (initially proposed by Ashby [46]), which describes an inverse feature size dependence of the strengthening effect. Additionally, an increase of the maximum stress can be observed for all samples when HPT pre-deformation is applied. Based on the same strain gradient theory, the HPT generated hardening indicates that inhomogeneous glass features have already been formed during the plastic deformation of the HPT process. The Young's moduli calculated from the different pillar compression tests show large scatter and are at least a factor of 2–5 times smaller than the Young's moduli (E = 103–117 GPa) reported in the literature for Cu-Zr-Al metallic glasses with similar composition [47]. This discrepancy between macroscopic compression and micropillar compression tests may be resolved by taking into account the misalignment (buckling) of the pillars since the compression tests were not ideally uniaxial. Micropillar misalignment originates mainly from inhomogeneous internal stresses, which are present in most materials (except high purity single crystals) and released partially by sample distortions during pillar fabrication. This concept is supported by the observation, that HPT samples should contain large stress inhomogeneities due to the pre-deformation induced dense shear band structure [24].

To quantify the misalignments, SEM images acquired during the in-situ pillar compression were analyzed and both in-axis and off-axis deformations were measured visually (see Fig. 2c and d). Fig. 7 shows the time dependence of this off-axis strain ($\gamma(t)$) with the in-axis strain

($\varepsilon_{in}(t)$) and the experimental indenter strain ($\varepsilon_{exp}(t)$) for all the tests. Comparing the off-axis strains with the difference of in-axis and experimental strains, we can state that γ correlates with the difference of ε_{in} and ε_{exp}. For as-cast samples, ε_{in} and ε_{exp} nearly overlap and there is only a small difference in the slopes. While the HPT samples, which exhibit higher initial γ_0 misalignment compared to the as-cast samples, show large difference between ε_{in} and ε_{exp}. The difference is especially clear in the initial part of these curves.

This indicates the presence of an additional in-axis elastic deformation due to the initial small off-axis misalignment. Therefore, off-axis deformation, i.e. the buckling of the micropillars, cannot be neglected and the buckling effect significantly modifies the elastic behavior of the indenter pillar system. Similar difference between the microscopically measured and macroscopic moduli is very common in deformation tests disclosed in the literature.

4.2. Acoustic emission signal and shear band formation

Size effects have been observed in various deformation characteristics of the present micro-pillar compression tests. Change in the sample shape was observed for both the as-cast and HPT pre-deformed micropillars. For larger micropillars single shear band fracture was observed, while micropillars with 4 μm size exhibited plastic deformability by having multiple shear bands (Fig. 3). Similarly, the plastic regime of the deformation curves (Fig. 5) have changed as a function of micropillar size. These observations are in qualitative agreement with the literature on MG micropillar deformation [25–28]. Although each test was unique in the present compression series, the above statements are independent of either the size parameter or the deformation state, therefore, the statements were deduced from the results of either 2 or 3 compression tests.

The sum of the total elastic energy in the sample and the surface energy of a plane defect exhibits a maximum as a function of defect size (2d) at a given σ external stress. Based on the Griffith theory [48], this maximum occurs at a critical defect size,

$$d_{crit} = \frac{2E\Gamma}{\sigma^2}, \qquad (1)$$

where E is the Young's modulus and Γ is the specific surface energy. As a rule of thumb, a shear band above such a critical size becomes unstable
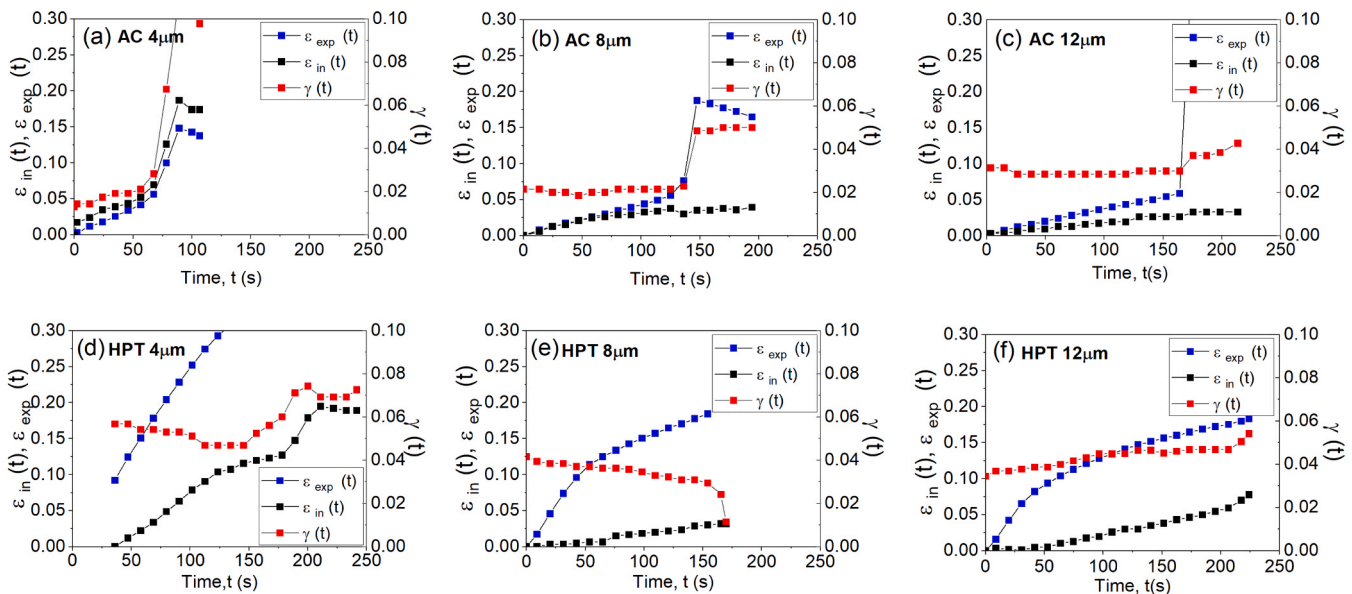

Fig. 7. Time dependence of experimental strain ($\varepsilon_{exp}(t)$) and optical strain ($\varepsilon_{in}(t)$) with off axis displacement ($\gamma(t)$) for the 4, 8, and 12 μm pillar sizes in the as-cast (a-c) and HPT deformed samples (d-f), respectively.

in a MG and is able to extend to minimize the total energy [25,28]. When sample size is small, i.e. it is $a_{crit} < d_{crit}/\sqrt{2}$, shear band formation is energetically impeded and homogeneous plastic flow can be observed [26]. For the present micropillar compression tests $d_{crit} \approx 50$ nm is estimated based on $E \approx 110$ GPa [47], $\Gamma \approx 1$ J/m2 [26] and $\sigma = \sigma_{yield} \approx 2.1$ GPa (see Table 1). Accordingly, unstable shear band formation (regimes II or III [33]) can be predicted beyond the yield point for all deformation tests of the present work. The Griffith theory also predicts unstable shear band growth below the yield stress as the theory basically bases on a linear elastic approach. Therefore, Eq. 1 is valid also in the elastic regime. A critical stress $\sigma_{crit} = \sqrt{\frac{\sqrt{2}2E\Gamma}{a}}$ can also be calculated from Eq. 1 ($\sigma_{crit} = 0.3, 0.2$ and 0.15 GPa for $a=4, 8$ and 12 μm size pillars, respectively, cf. with Fig. 5). Above the critical stress the largest preexisting defects should lead to shear band formation well below the yield point of the material.

Since AE events signal shear band nucleation [35] and are in exact correlation with the formation of shear bands [41], the AE events in Fig. 5 indicate shear band formation not only beyond the yield point, but also in the elastic regime for $\sigma < \sigma_{crit}$. The observed AE events are in good agreement with the predicted low critical stresses in the elastic regime of the 8 and 12 μm size as-cast pillars (see Fig. 5b and c). The maximum amplitude of these tests show approximately a^2 dependence, which predict a smaller AE amplitude than the AE detection limit for the 4 μm pillars. Hence, similar AE events are practically invisible for the smallest pillars in our experiments. The size dependence indicates that these AE events in the elastic regime form around the SBs in a slab like volume which has much smaller thickness than the sample size.

Interestingly, micropillars fabricated from the pre-deformed samples show weaker AE signal both in the elastic regime and beyond the yield point (see Fig. 5d-f). This indicates that either fewer shear bands form or shear band formation is less synchronized in time due to the pre-deformation. Reduction of strain localization though structural rejuvenation, i.e. activation of the glass state due to increased disorder, was observed recently in similar Cu-Zr-Al BMGs deformed by HPT [49] in agreement with the present observations. However, the synchronization and, hence, AE signal formation seems to be more regular in the HPT sample (cf. Fig. 6a and b), which reports about the larger effect of random structural features on the synchronization of AE events in the as-cast material.

Beside the activation due to the stored extra elastic energy in pre-deformed MGs, as-cast and pre-deformed pillars have also an inherent difference in terms of the homogeneity of internal stresses [23]. As-cast pillars are supposed to be relatively homogeneous and lack internal stress fluctuations, therefore the whole pillar is in the same stress state. Hence larger sample volume can take place in shear band formation in a synchronized way. On the contrary, stress inhomogeneities exist down to sub-micrometer size due to the dense shear band structure in HPT deformed MGs [23,24]. Such inhomogeneity can induce misorientation and inhomogeneity also in shear band formation and may lead to the appearance of higher number, shorter and asynchronized shear bands segments producing weaker AE signal. This presumption is also in agreement with the observed plasticity and inhomogeneous shear banding in HPT pre-deformed macroscopic tensile tests [14].

Finally, the different deformation history of the as-cast and HPT samples can induce structural differences by rejuvenation in the glass. These structural differences have effect at the beginning of the shear band formation due to the different strain gradients as it was showed in a molecular dynamic study by Tian et al. [50]. In timing, these effects can be separated from the serrations and the shear band movement; and can be best captured by the AE signal (Figs. 5 and 6). Rejuvenation and in-homogeneity can also be induced by other deformation methods with no constraint [51] and even by simple elastostatic loading [52]. Generally, the rejuvenated MG samples show better ductility, i.e. improved resistance against fracture [51,52] along unstable shear bands. Based on the presence of AE signal in the elastic regime of micro compression tests

(Fig. 5) and the inherent behavior of the rejuvenation process in glasses [53], we propose that rejuvenation has significant effect also on the stabilization of the unstable shear bands below the yield point.

4.3. Effects of environment on shear band propagation

Unstable shear band formation is generally followed by continuously increase in shear offset (shear band propagation) with no AE signal [41]. Those bands, which intersects the whole cross-section of a macroscopic sample, often reach large offsets comparable with the sample size (see e. g. the present micro compression tests with the 12 μm size micro-pillars in Fig. 3c and f). Initially, at the nucleation of the band, the strength of the shear band is comparable to the strength of the surrounding glassy material and later it decreases gradually as shear band propagation occurs in a fraction of seconds. The dynamics of this process depends strongly on the surrounding elastic environment. Since intense localized shear deformation relaxes, the external stress in the whole system and shear deformation of a shear band is an extremely stress sensitive process (it is a highly nonlinear process in the non-Newtonian regime of the plastic flow), stress variation can have a huge effect on shear banding and the formation of other shear bands in the material.

The elastic environment, i.e. the sample modulus and deformation machine compliance, can be described by a common K spring constant,

$$\frac{1}{K} = \frac{1}{K^* + \frac{L}{E_{exp}A}}, \tag{2}$$

where $K^* = 17$ mN/μm is the spring constant of the present deformation machine, $A = a^2$ is the cross section of the micropillar. After shear band formation the local stress can be expressed as

$$\sigma = \frac{F - K\sin(\alpha)\Delta x}{A - a\cos(\alpha)\Delta x} = \frac{\sigma_{yield} - K/a\sin(\alpha)(\Delta x/a)}{1 - \cos(\alpha)(\Delta x/a)}, \tag{3}$$

where F is the external force, α measures the orientation angle of the shear band from the compression axis, $\sigma_{yield} = F/A$ is the stress at the moment of band nucleation and Δx is the shear offset. As it can be seen from Eq. 3, the shear offset will have two opposite effects on the local stress. On one hand, the active cross-section of the sample will decrease with Δx, which increases the stress. On the other hand, Δx shear offset will lead to instant relaxation of the load in the sample because of the
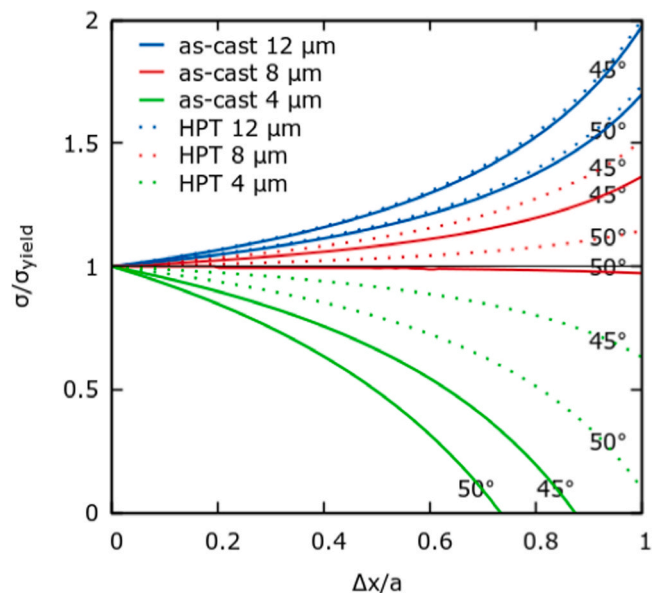

Fig. 8. Stress evolution during shear band offset for all micropillar compression tests, the lower and upper bounding curves of each measurement corresponds to $\alpha = 50$ and $\alpha = 45$ deg shear band angles, respectively.

displacement of the machine's cross-head. Fig. 8 shows the stress along the shear band as a function of the shear offset for the different test and sample parameters (a and E_{exp}) of the present micro-compression tests. As seen, the local stress can either increase or decrease with Δx depending mainly on the sample size based on Eq. 3. The boundary between the two opposite behavior (i.e. $\sigma = 0$) can provide another a_{crit}^* critical sample size,

$$a_{crit}^* = \frac{K \cdot tg(\alpha)}{\sigma_{yield}}, \tag{4}$$

which is close to 8 μm for the present test parameters (see Fig. 8a). Whereas in the calculation of $\sigma(\Delta x)$, the $\alpha = 45^o - 50^o$ range was supposed (higher angle corresponds to the lower bound in σ) and the effect of sample misalignment was taken into account by using the experimental compression moduli (Table 1).

It is also seen in Fig. 8 that for large samples ($a > a_{crit}^*$), the stress increase is monotonous in Δx and it diverges when the offset crosses the whole sample. This monotonous increasing behavior leads to positive feedback of the stress and results in fracture during shear band propagation, which is typical for macroscopic samples. In microscopic samples, i.e. for micropillar tests with adequately small sample size, $a < a_{crit}^*$, the stress decreases with Δx and becomes zero at a finite shear band offset. This negative feedback reduces the stress rapidly and stops shear band propagation temporarily even if local softening takes place along the shear band. Comparing the lower and upper bounds in α for slightly different shear band angles, the stress curves show strong sensitivity on the details, especially for the smaller pillar sizes. Accordingly, mostly, stress increase occurs in the 12 and 8 μm pillars, while the stress decreases in the 4 μm pillars during the operation of each shear band. Although, with special shear band parameters ($\alpha \approx 50^o$) the as-cast 8 μm pillar can show stable shear banding (cf. with Fig. 3). Here we should note that the compliance of the deformation machine is crucial in the unstable deformation behavior of shear bands (see Eq. 4). For extremely high spring constants ($K^* \rightarrow \infty$), Eq. 2 simplifies to $K \approx E_{exp} A/L$, which corresponds to a stress decrease during shear band propagation in Eq. 4 independent of the sample size. This extreme sensitivity of shear banding to the machine spring constant qualitatively explains the large scatter of the critical sample sizes in the literature. Nevertheless, it is in very good quantitative agreement with the observed size dependent deformation mechanism in the present micropillar compression tests.

5. Conclusions

Micro-compression tests coupled with in-situ SEM-imaging and simultaneous AE-signal detection have been carried out on $Cu_{38}Zr_{54}Al_8$ glassy and pre-deformed micropillars of different sizes. Micro-compression tests promoted the formation of shear bands irrespective of the sample size and preliminary deformation, which is in agreement with the prediction of the shear band formation model based on the Griffith theory. However, a clear size effect was detected with improved plasticity, more serrations, but weaker AE signal with small pillar sizes, which can be explained quantitatively by the size dependent compliance of the pillar/indenter systems.

Pillars made of the pre-deformed metallic glass sample have larger initial misalignments (induced by the rejuvenated structure and stress inhomogeneities) and showed differences in plastic behavior due to the larger off axis deformation. AE signal was detected already during the linear elastic regime in the as-cast pillars, while this signal was significantly weaker for the rejuvenated structure of the pre-deformed metallic glass. Nevertheless, clear correlation was observed between the stress drops and the AE signal for all the samples. Based on this correlation and absence of AE signal in the elastic regime of the rejuvenated glass, we propose that rejuvenation is ubiquitous in the glass structure and should have significant role on the stabilization of unstable shear bands below the yield point.

CRediT authorship contribution statement

Talaye Arjmandabasi: Data curation, Investigation, Methodology, Visualization, Writing – original draft. **Dávid Ugi:** Investigation (in-situ SEM, AE). **Ádám Révész:** Investigation (HPT), Writing – review & editing. **Erhard Schafler:** Investigation (HPT), Writing – review & editing. **David J. Browne:** Conceptualization, Writing – review & editing. **Zsolt Kovács:** Conceptualization, Data curation, Formal analysis, Investigation, Methodology, Resources, Validation, Visualization, Writing – original draft, Writing – review & editing.

Declaration of Competing Interest

The authors declare the following financial interests/personal relationships which may be considered as potential competing interests: Talaye Arjmandabasi reports financial support was provided by Tempus Public Foundation.

Data Availability

Data will be made available on request.

References

[1] F. Spaepen, A microscopic mechanism for steady state inhomogeneous flow in metallic glasses, Acta Metall. 25 (1977) 407–415, https://doi.org/10.1016/0001-6160(77)90232-2.

[2] A.S. Argon, Plastic deformation in metallic glasses, Acta Met. 27 (1979) 47–58, https://doi.org/10.1016/0001-6160(79)90055-5.

[3] A. Inoue, Stabilization of metallic supercooled liquid and bulk amorphous alloys, Acta Mater. 48 (2000) 279–306, https://doi.org/10.1016/S1359-6454(99)00300-6.

[4] A.G. Murphy, P. Meagher, A. Norman, D.J. Browne, Mechanical and thermal stability of bulk metallic glass alloys identified as candidates for space mechanism applications, Mater. Des. 224 (2022), 111350, https://doi.org/10.1016/j.matdes.2022.111350.

[5] G. Kumar, H.X. Tang, J. Schroers, Nanomoulding with amorphous metals, Nature 457 (2009) 868–872, https://doi.org/10.1038/nature07718.

[6] W. Klement, R.H. Willens, P. Duwez, Non-Crystalline structure in solidified gold-silicon alloys, Nature 187 (1960) 869–870, https://doi.org/10.1038/187869b0.

[7] C.A. Pampillo, Localized shear deformation in a glassy metal, Scr. Mater. 6 (1972) 915–917.

[8] M.W. Chen, A. Inoue, W. Zhang, T. Sakurai, Extraordinary plasticity of ductile bulk metallic glasses, Phys. Rev. Lett. 96 (2006), 245502, https://doi.org/10.1103/PhysRevLett.96.245502.

[9] C.A. Schuh, T.C. Hufnagel, U. Ramamurty, Mechanical behavior of amorphous alloys, Acta Mater. 55 (2007) 4067–4109, https://doi.org/10.1016/j.actamat.2007.01.052.

[10] M. Miller, P. Liaw, Bulk Metallic Glasses, Springer Publishing, New York, 2008, https://doi.org/10.1007/978-0-387-48921-6.

[11] R.D. Conner, W.L. Johnson, N.E. Paton, W.D. Nix, Shear bands and cracking of metallic glass plates in bending, J. Appl. Phys. 94 (2003) 904, https://doi.org/10.1063/1.1582555.

[12] M. Ezzeldien, Zs Kovács, J. Lendvai, F. Chmelík, K. Máthis, Stages in room temperature torsional deformation of a Vitreloy bulk metallic glass, J. Alloy. Compd. 577 (2013) 25–29, https://doi.org/10.1016/j.jallcom.2013.04.103.

[13] Y. Zhang, W. Wang, A.L. Greer, Making metallic glasses plastic by control of residual stress, Nat. Mater. 5 (2006) 857–860, https://doi.org/10.1038/nmat1758.

[14] S.H. Joo, D.H. Pi, A.D.H. Setyawan, H. Kato, M. Janecek, Y.C. Kim, S. Lee, H. S. Kim, Work-Hardening Induced Tensile Ductility of Bulk Metallic Glasses via High-Pressure Torsion, Sci. Rep. 5 (2015) 9660, https://doi.org/10.1038/srep09660.

[15] R.Z. Valiev, R.K. Ishlamgaliev, I.V. Alexandrov, Bulk nanostructured materials from severe plastic deformation, Prog. Mater. Sci. 45 (2000) 103–189, https://doi.org/10.1016/S0079-6425(99)00007-9.

[16] K. Edalati, Z. Horita, A review on high-pressure torsion (HPT) from 1935 to 1988, Mater. Sci. Eng. A. 652 (2016) 325–352, https://doi.org/10.1016/j.msea.2015.11.074.

[17] Z.S. Kovács, P. Henits, A.P. Zhilyaev, Á. Révész, Deformation induced primary crystallization in a thermally non-primary crystallizing amorphous $Al_{85}Ce_8Ni_5Co_2$ alloy, Scr. Mater. 54 (2006) 1733–1737, https://doi.org/10.1016/j.scriptamat.2006.02.004.

[18] Á. Révész, S. Hóbor, P.J. Szabó, A.P. Zhilyaev, Z.S. Kovács, Deformation induced crystallization in an amorphous $Cu_{60}Zr_{20}Ti_{20}$ alloy by high pressure torsion, Mater. Sci. Eng. A. 460–461 (2007) 459–463, https://doi.org/10.1016/j.msea.2007.01.081.

[19] P. Henits, Á. Révész, A.P. Zhilyaev, Z.S. Kovács, Severe plastic deformation induced nanocrystallization of melt-spun $Al_{85}Y_8Ni_5Co_2$ amorphous alloy, J. Alloy. Compd. 461 (2008) 195–199, https://doi.org/10.1016/j.jallcom.2007.07.049.

[20] S. Hóbor, Á. Révész, P.J. Szabó, A.P. Zhilyaev, V.K. Kis, J.L. Lábár, Z.S. Kovács, High pressure torsion of amorphous $Cu_{60}Zr_{30}Ti_{10}$ alloy, J. Appl. Phys. 104 (2008), 033525, https://doi.org/10.1063/1.2964115.

[21] Á. Révész, E. Schafler, Z.S. Kovács, Structural anisotropy in a $Zr_{57}Ti_5Cu_{20}Al_{10}Ni_8$ bulk metallic glass deformed by high pressure torsion at room temperature, Appl. Phys. Lett. 92 (2008), 011910, https://doi.org/10.1063/1.2830992.

[22] Z.S. Kovács, E. Schafler, Á. Révész, Volume changes in Vitreloy bulk metallic glass during room temperature high-pressure torsion, J. Mater. Res 23 (2008) 3409–3414, https://doi.org/10.1557/JMR.2008.0416.

[23] K. Nakazawa, S. Lee, K. Niitsu, M. Kameyama, T. Sannomiya, S. Kohara, K. Mitsuishi, K. Tsuchiya, Nanoscale strain mapping and symmetry analysis of $Zr_{50}Cu_{40}Al_{10}$ metallic glass rejuvenated by high-pressure torsion via 4D scanning transmission electron microscopy, J. Non-Cryst. Solids 606 (2023) 122197, https://doi.org/10.1016/j.jnoncrysol.2023.122197.

[24] Z.S. Kovács, E. Schafler, P. Szommer, Á. Révész, Localization of plastic deformation along shear bands in Vitreloy bulk metallic glass during high pressure torsion, J. Alloy. Compd. 593 (2014) 207–212, https://doi.org/10.1016/j.jallcom.2014.01.079.

[25] A. Dubach, R. Raghavan, J.F. Löffler, J. Michler, U. Ramamurty, Micropillar compression studies on a bulk metallic glass in different structural states, Scr. Mater. 60 (2009) 567–570, https://doi.org/10.1016/j.scriptamat.2008.12.013.

[26] C.A. Volkert, A. Donohue, F. Spaepen, Effect of sample size on deformation in amorphous metals, J. Appl. Phys. 103 (2008), 083539, https://doi.org/10.1063/1.2884584.

[27] H. Guo, P.F. Yan, Y.B. Wang, J. Tan, Z.F. Zhang, M.L. Sui, E. Ma, Tensile ductility and necking of metallic glass, Nat. Mater. 6 (2007) 735–739, https://doi.org/10.1038/nmat1984.

[28] D. Jang, J.R. Greer, Transition from a strong-yet-brittle to a stronger-and-ductile state by size reduction of metallic glasses, Nat. Mater. 9 (2010) 215–219, https://doi.org/10.1038/nmat2622.

[29] Y. Teng, Z.D. Sha, Uncovering the Inherent Size Dependence of Yield Strength and Failure Mechanism in Micron-Sized Metallic Glass, Materials 15 (2022) 6362, https://doi.org/10.3390/ma15186362.

[30] Y.H. Lai, H.M. Chen, C.J. Lee, J.C. Huang, J.S.C. Jang, Strain burst speeds in metallic glass micropillars, Intermetallics 18 (2010) 1893–1897, https://doi.org/10.1016/j.intermet.2010.02.037.

[31] J.M. Wheeler, R. Raghavan, J. Michler, Temperature invariant flow stress during micro compression of a Zr-based bulk metallic glass, Scr. Mater. 67 (2012) 125–128, https://doi.org/10.1016/j.scriptamat.2012.03.039.

[32] O.V. Kuzmin, Y.T. Pei, C.Q. Chen, J.T.M.De Hosson, Intrinsic and extrinsic size effects in the deformation of metallic glass nanopillars, Acta Mater. 60 (2012) 889–898, https://doi.org/10.1016/j.actamat.2011.11.023.

[33] R. Qu, D. Tönnies, L. Tian, Z. Liu, Z. Zhang, C.A. Volkert, Size-dependent failure of the strongest bulk metallic glass, Acta Mater. 178 (2019) 249–262, https://doi.org/10.1016/j.actamat.2019.08.019.

[34] T. Tabbakh, A. Kurdi, A.K. Basak, Effect of Strain Rate and Extrinsic SIZE Effect on Micro-Mechanical Properties of Zr-Based Bulk Metallic Glass (https://doi.org/doi:), Metals 11 (2021) 1611, https://doi.org/10.3390/met11101611.

[35] A.Yu Vinogradov, V.A. Khonik, Kinetics of shear banding in a bulk metallic glass monitored by acoustic emission measurements, Philos. Mag. 84 (21) (2004) 2147–2166, https://doi.org/10.1080/14786430410001678217.

[36] Á. Hegyi, P.D. Ispánovity, M. Knapek, D. Tüzes, K. Máthis, F. Chmelík, Z. Dankházi, G. Varga, I. Groma, Micron-Scale Deformation: A Coupled In Situ Study of Strain Bursts and Acoustic Emission, Microsc. Microanal. 23 (2017) 1076–1081, https://doi.org/10.1017/S1431927617012594.

[37] P.D. Ispánovity, D. Ugi, G. Péterffy, M. Knapek, S.Z. Kalácska, D. Tüzes, Z. Dankházi, K. Máthis, F. Chmelík, I. Groma, Dislocation avalanches are like earthquakes on the micron scale, Nat. Commun. 13 (2022) 1975, https://doi.org/10.1038/s41467-022-29044-7.

[38] C.B. Scruby, An introduction to acoustic emission, J. Phys. E: Sci. Instrum. 20 (1987) 946–953, https://doi.org/10.1088/0022-3735/20/8/001.

[39] C.R. Heiple, S.H. Carpenter, Acoustic emission produced by deformation of metals and alloys, A review, J. Acoust. Emiss. 6 (1987) 177–204.

[40] A. Lazarev, A. Vinogradov, S. Hasimotho, Comparative analysis of inhomogeneous plastic flow in bulk and ribbon metallic glasses monitored by acoustic emission, J. Alloy. Compd. 504S (2010) S60–S64, https://doi.org/10.1016/j.jallcom.2010.02.076.

[41] F.H. Dalla Torre, D. Klaumünzer, R. Maaß, J.F. Löffler, Stick–slip behavior of serrated flow during inhomogeneous deformation of bulk metallic glasses, Acta Mater. 58 (2010) 3742–3750, https://doi.org/10.1016/j.actamat.2010.03.011.

[42] S.N. Aqida, D. Brabazon, S. Naher, Z. Kovacs, D.J. Browne, Laser micro-processing of amorphous and partially crystalline Cu45Zr48Al7 alloy, Appl. Phys. A 101 (2010) 357–360, https://doi.org/10.1007/s00339-010-5829-3.

[43] D.J. Stratton, C. Byrne, J. Mulcahy, D.J. Browne, Sub-Micron Feature Patterning of Thermoplastics using Multi-Scale BMG Tooling, MRS Online Proc. Libr. 1300 (2011) 208, https://doi.org/10.1557/opl.2011.273.

[44] Á. Révész, T. Arjmandabasi, E. Schafler, D.J. Browne, Z.S. Kovács, Comprehensive thermal analysis of a high stability Cu-Zr-Al bulk metallic glass subjected to high-pressure torsion, J. Therm. Anal. Calorim. 148 (2023) 2323–2334, https://doi.org/10.1007/s10973-022-11875-7.

[45] R.Z. Valiev, Y. Estrin, Z. Horita, T.G. Langdon, M.J. Zehetbauer, Y.T. Zhu, Producing bulk ultrafine-grained materials by severe plastic deformation, JOM 58 (2006) 33–39, https://doi.org/10.1007/s11837-006-0213-7.

[46] M.F. Ashby, The deformation of plastically non-homogeneous materials, Philos. Mag. 21 (1970) 399–424.

[47] T.L. Cheung, C.H. Shek, Thermal and mechanical properties of Cu–Zr–Al bulk metallic glasses, J. Alloy. Compd. 434–435 (2007) 71–74, https://doi.org/10.1016/j.jallcom.2006.08.109.

[48] A.A. Griffith, The phenomena of rupture and flow in solids, Philos. Trans. R. Soc. Lond. A 221 (1921) 163–198, https://doi.org/10.1098/rsta.1921.0006.

[49] F. Meng, K. Tsuchiya, M.J. Kramer, R.T. Ott, Reduction of shear localization through structural rejuvenation in Zr–Cu–Al bulk metallic glass, Mater. Sci. Eng. A 765 (2019), 138304, https://doi.org/10.1016/j.msea.2019.138304.

[50] Z.-L. Tian, Y.-J. Wang, Y. Chen, L.-H. Dai, Strain gradient drives shear banding in metallic glasses, Phys. Rev. B 96 (2017), 094103, https://doi.org/10.1103/PhysRevB.96.094103.

[51] R.M.O. Mota, E.T. Lund, S. Sohn, D.J. Browne, D.C. Hofmann, S. Curtarolo, A. van de Walle, J. Schroers, Enhancing ductility in bulk metallic glasses by straining during cooling, Comm. Mater. 2 (2021) 23, https://doi.org/10.1038/s43246-021-00127-0.

[52] S. Zhang, B. Shi, J. Wang, Y. Xu, P. Jin, Rejuvenation of a naturally aged bulk metallic glass by elastostatic loading, Mater. Sci. Eng. A 806 (2021), 140843, https://doi.org/10.1016/j.msea.2021.140843.

[53] S.V. Ketov, Y.H. Sun, S. Nachum, Z. Lu, A. Checchi, A.R. Beraldin, H.Y. Bai, W.H. Wang, D.V. Louzguine-Luzgin, M.A. Carpenter, A.L. Greer, Rejuvenation of metallic glasses by non-affine thermal strain, Nature 524 (2015) 200–203, https://doi.org/10.1038/nature14674.